DESY 93-185
December 1993

ISSN 0418-9833

Electron/Pion Separation with the H1 LAr Calorimeters

H1 Calorimeter Group

Abstract

The performances of the H1 liquid argon calorimeter modules for the energy measurements and identification of electrons are studied with test data taken at CERN in the energy range 5 to 166 GeV.

Various electron identification estimators exploiting global or detailed shower characteristics are studied and compared. The usage impact position measurements is also discussed. A best combination of robust shower estimators leads typically to π misidentification probabilities in the range 1.5 to 5.0×10^{-3} at 30 GeV for 95 % electron detection efficiency. This further reduces to $\sim 10^{-4}$ for these pions to be misidentified as electrons below 25 GeV.

Submitted to NIM

H1 Calorimeter Group

B. Andrieu[10], J. Bán[6], E. Barrelet[11], G. Bernardi[11], M. Besançon[4], E. Binder[5], H. Blume[8], K. Borras[3], V. Boudry[10], V. Brisson[9], A. Campbell[5], T. Carli[8], M. Colombo[3], Ch. Coutures[4], G. Cozzika[4], J. Cvach[10], M. David[4], L. Del Buono[11], B. Delcourt[9], M. Devel[9], P. Dingus[10], A. Drescher[3], J. Duboc[11], R. Ebbinghaus[3], S. Egli[14] J. Feltesse[4], Z.Y. Feng[11], W. Flauger[5,†], M. Flieser[8], K. Gamerdinger[8], J. Gayler[5], L. Goerlich[2], M. Goldberg[11], R. Grässler[1], H. Greif[8], M. Haguenauer[10], L. Hajduk[2], O. Hamon[11], P. Hartz[3], R. Haydar[9], W. Hildesheim[11], N. Huot[11], M.A. Jabiol[4], A. Jacholkowska[9], M. Jaffre[9], H. Jung[1], C. Kiesling[8], H. Kolanoski[3], V. Korbel[5], M. Korn[3], W. Krasny[2], J.P. Kubenka[8], J. Kurzhöfer[3], H. Küster[5], J.F. Laporte[4], U. Lenhardt[3], P. Loch[5], D. Lüers[8,†], J. Marks[5], J. Martyniak[2], T. Merz[5], H.K. Nguyen[11], H. Oberlack[8], U. Obrock[3], C. Pascaud[9], S. Peters[8], K. Rauschnabel[3], P. Ribarics[8], M. Rietz[1], M. Rudowicz[8], V. Rusinov[7], N. Sahlmann[1], E. Sanchez[8], P. Schacht[8], V. Shekelyan[7], Y. Sirois[10], P. Staroba[12], H. Steiner[11], U. Straumann[14] J. Turnau[2], L. Urban[8], C. Vallee[11], M. Vecko[10,12], P. Verrecchia[4], G. Villet[4], D. Wegener[3], H. P.Wellisch[8], T.P. Yiou[11], J. Žáček[9,13], and Ch. Zeitnitz[5]

[1] *III. Physikalisches Institut der RWTH, Aachen, Germany*[a]
[2] *Institute for Nuclear Physics, Cracow, Poland*[b]
[3] *Institut für Physik, Universität Dortmund, Dortmund, Germany*[a]
[4] *DAPNIA, Centre d'Etudes de Saclay, Gif-sur-Yvette, France*
[5] *DESY, Hamburg, Germany*
[6] *Institute of Experimental Physics, Slovak Academy of Sciences, Košice, Slovak Republic*
[7] *Institute for Theoretical and Experimental Physics, Moscow, Russia*
[8] *Max-Planck-Institut für Physik, München, Germany*[a]
[9] *LAL, Université de Paris-Sud, IN2P3-CNRS, Orsay, France*
[10] *LPNHE, Ecole Polytechnique, IN2P3-CNRS, Palaiseau, France*
[11] *LPNHE, Universités Paris VI and VII, IN2P3-CNRS, Paris, France*
[12] *Institute of Physics, Czech Academy of Sciences, Praha, Czech Republic*
[13] *Nuclear Center, Charles University, Praha, Czech Republic*
[14] *Physik-Institut der Universität Zürich, Zürich, Switzerland*[c]

[†] *Deceased*

[a] *Supported by the Bundesministerium für Forschung und Technologie, FRG, under contract numbers 6AC47P, 6DO57I and 6MP17I*
[b] *Supported by the Polish State Committee for Scientific Research, grant No. 204209101*
[c] *Supported by the Swiss National Science Foundation*

1 Introduction

The lead/stainless steel-liquid argon (LAr) calorimeter [1] of the H1 experiment [2] at the HERA ep collider is finely segmented to optimally recognize and measure electromagnetic (e.m.) showers. Some of the calorimeter modules were tested in their final designs at CERN in 1989-1990 in an energy range not unlike that of the scattered electrons in deep inelastic scattering events at HERA. The aim was to derive energy calibration functions for electrons [3], hadrons and jets [4] and to study electron/hadron separation. Some early results concerning e/π separation were discussed in [5]. Here, we present our complete results on e/π separation performances studied for four module configurations.

The test set-up, module configurations and data sets are presented in sections 2 to 4. The analysis and results are presented in section 5. The section 5.1 introduces a simple clustering algorithm which determines the measurement envelopes for electron-induced showers and electron isolation. The linearity and resolutions for electron energy measurements and the e/π separation results obtained from calorimetry information restricted to the electron envelope are presented in sections 5.2 and 5.3 while the separation performances obtained using all available information within the isolation cone are presented in section 5.4. In the context of the actual H1 experiment, different physics analysis applications may require different combinations of electron estimators exploiting global or detailed shower characteristics. Hence, various sets of calorimetric estimators are considered as well as combinations using the independent information on the direction of the incident particles.

2 Experimental set-up

The LAr modules were installed in a cryostat on the H6 beam line of the CERN North Area. The layout of the beam telescope and H1 detector configuration is shown in fig. 1. The beam

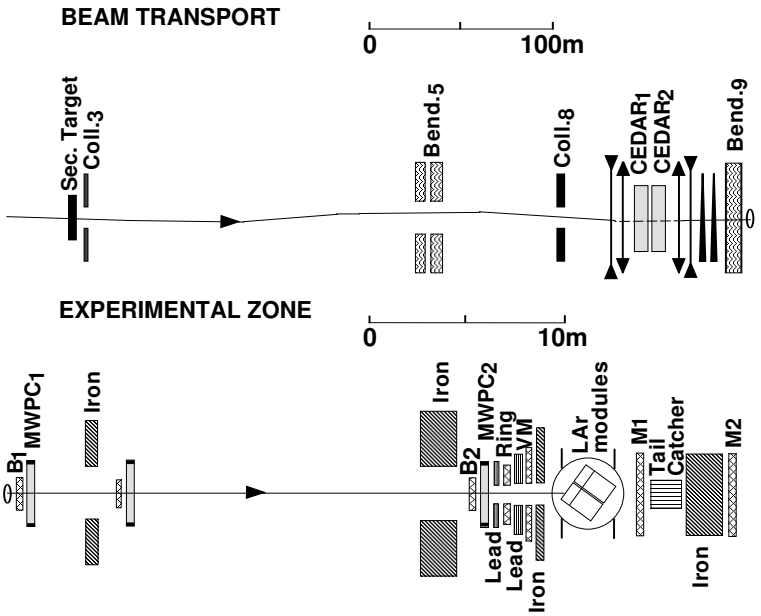

Figure 1: *Schematic representation of the beam transport* (top) *and H1 experimental set-up* (bottom) *during the* CERN *test runs. The small oval symbol marks the end of the vacuum beam pipes at the beginning of the experimental zone.*

line was mostly operated in a tertiary mode [6] with mixed e^+ and π^+ in the energy range 10 to 80 GeV produced in a 1 m polyethylene secondary target and transported over 370 m up to the experimental zone (fig. 1 top). In this mode, the π^+ beam fraction increases roughly linearly with energy from about 10 ± 5 % at 10 GeV to 70 ± 5 % at 80 GeV. The momentum spread controlled by the aperture of a pair of collimators (coll. 3 and 8 in fig. 1) was kept to $\Delta P/P \lesssim 0.5\%$. The beam energies above 80 GeV are achieved by operating in a secondary mode.

For the data taking, the arrival of a beam particle was signalled by a coincidence between a pair of scintillators (B_1 and B_2 on fig. 1 bottom), each having a thickness of 1.25 cm and a cross-section of $3 \times 3\,\mathrm{cm}^2$. The beam halo was rejected by asking for an anti-coincidence with a veto wall (VM) of scintillator counters. This together with an additional cut on the maximal signal in a ring scintillator limited the acceptance for the beam to a useful area of about $\pi \times 1.5^2\,\mathrm{cm}^2$. Two multiwire proportional chambers ($\mathrm{MWPC}_{1,2}$) each with one horizontal and one vertical anode plane of wires were used to monitor the beam profile and to veto upstream showers. All planes had wire-to-wire spacing of 2 mm. The MWPC_2 is placed at 1.9 m in front of the cryostat. The beam spot measured with the MWPC chambers has a $\sigma_x \times \sigma_y$ size varying from $\sim 0.5\,\mathrm{cm}^2$ at 10 GeV to $\sim 0.2\,\mathrm{cm}^2$ at 80 GeV.

The nature of the incoming particle was determined by the triggering of two Čerenkov differential counters with achromatic ring focus (CEDAR) [7] which are well adapted to the above mentioned energy range in the tertiary mode, with a low energy operational limit for π's around 8 GeV due to the maximal allowed radiator gas pressure and an upper limit due to the minimal angular separation needed for the e and π's Čerenkov rings around 95 GeV. Muons originating mainly from pion decay in flight were rejected by requiring an anti-coincidence with a scintillator veto wall (M2) placed behind the LAr cryostat after an additional 14 nuclear interaction lengths (λ_I) of material.

More details on the beam detectors and trigger system can be found in [8, 9], where test results of early prototype modules were presented.

3 Calorimeter modules configurations

The e and π single particle data were taken over four test periods each with a different pair of LAr modules having the materials, the read-out cell structure and the segmentation of the final H1 design [1]. Moreover, as illustrated in fig. 2, the impact points and angles were chosen to correspond to realistic conditions for similar modules in the full H1 set-up. In the three first periods (i.e. module configurations) an octant of two neighbouring central or forward barrel wheels, namely the FB1/FB2, CB3/FB1 and CB2/CB3 wheels, were put into the cryostat. In the fourth period, a quarter of the Inner Forward end-cap (IF) was used. As seen in fig. 2, the segmentation of the electromagnetic (e.m.) and hadronic stacks varies from the CB to the IF wheel. Before penetrating the fiducial volume of the calorimeter stacks in the CERN set-up, the beam particles had to travel through 0.24 radiation length (X_0) of inactive material (air and beam detectors) up to MWPC_2, then $0.32\,\mathrm{X}_0$ through the cryostat stainless steel entrance window, and finally through LAr and LAr-excluder (Rohacell) material; for a total of about $1\,\mathrm{X}_0$ in the FB1/FB2 configuration, $0.8\,\mathrm{X}_0$ for CB3/FB1, $0.7\,\mathrm{X}_0$ for CB2/CB3 and $1.5\,\mathrm{X}_0$ for IF. The main characteristics of the four types of modules which were hit by the incident beams at CERN are given in table 1. For a given energy and module configuration, the electron and pion runs were taken at similar beam and impact positions.

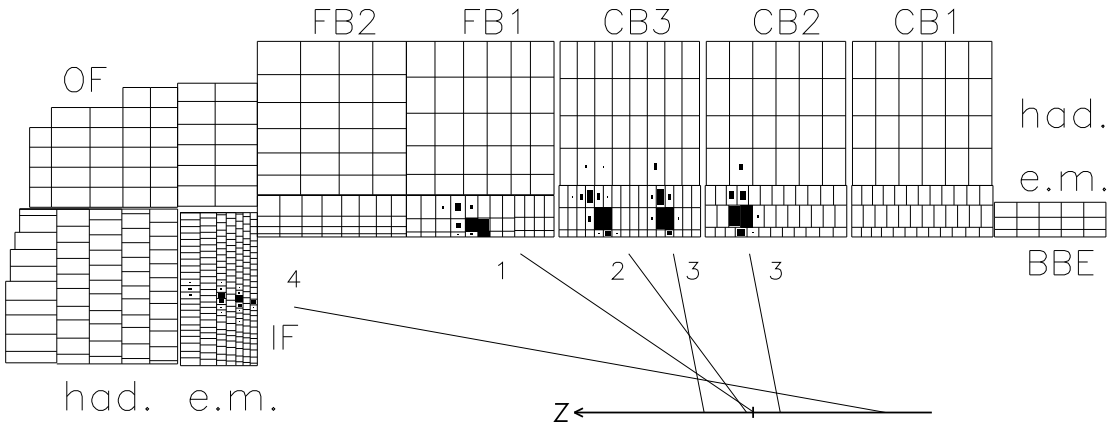

Figure 2: *Schematic representation of the impact directions in each of the four test configurations as viewed in the $r-z$ coordinates of half a cylinder of the* H1 *set-up at* HERA. *The vector segments are drawn from the distance of closest approach to the z axis to the calorimeter impact point.*

Module	Electromagnetic section $\overline{\mathrm{X}}_0 \simeq 1.6\,\mathrm{cm}$ $\overline{\mathrm{R}}_\mathrm{m} \simeq 3.6\,\mathrm{cm}$ $\overline{\epsilon}_\mathrm{c} \simeq 9.5\,\mathrm{MeV}$ $\overline{\lambda}_\mathrm{I} \simeq 31.\,\mathrm{cm}$						Hadronic section $\overline{\mathrm{X}}_0 \simeq 2.5\,\mathrm{cm}$ $\overline{\mathrm{R}}_\mathrm{m} \simeq 2.6\,\mathrm{cm}$ $\overline{\epsilon}_\mathrm{c} \simeq 21.4\,\mathrm{MeV}$ $\overline{\lambda}_\mathrm{I} \simeq 21.\,\mathrm{cm}$			
	$\Delta L/\overline{\mathrm{X}}_0$				$\sqrt{S}/\overline{\mathrm{R}}_\mathrm{m}$	Total	$\Delta L/\overline{\mathrm{X}}_0$	$\sqrt{S}/\overline{\mathrm{R}}_\mathrm{m}$	Nb. of	Total
	k=0	k=1	k=2	k=3		$N_\mathrm{cell}^\mathrm{em}$	k=0		layers	$N_\mathrm{cell}^\mathrm{had.}$
CB2	3.6	8.4	7.6	-	2.4	288	8.	5.3	4	192
CB3	2.7	8.4	8.5	-	1.4	768	8.	4.6	4	256
FB1	2.2	5.0	8.4	-	1.8	576	5.	5.8	5	240
IF	3.0	5.4	7.2	13.0	1.0	≈ 1300	6.5	3.4	5	320

Table 1: *Segmentation of the LAr modules. The mean Moliere radius $\overline{\mathrm{R}}_\mathrm{m}$, radiation length $\overline{\mathrm{X}}_0$, critical energy $\overline{\epsilon}_\mathrm{c}$ and interaction length $\overline{\lambda}_\mathrm{I}$ are given for the e.m. and hadronic sections. The mean longitudinal and lateral sizes of e.m. and hadronic (1^{rst} layer) cells and the total number $N_{cell}^{e.m.}$ ($N_{cell}^{had.}$) of e.m. (hadronic) cells in one "octant" ($\Delta\phi = 45°$) are given for each module. ΔL is the thickness of a layer and S the mean surface of a cell.*

4 Signal processing and data sets

The electronic chain for the online treatment of the LAr pulses is described in detail in [8]. Offline, all data are first pre-processed to bring the LAr signals to an "electromagnetic scale"; i.e. a scale corresponding to a calibration of both the e.m. and hadronic sections with electrons.

The signal in each cell is first corrected for pedestal offset and then converted from ADC counts to charge using a third order polynomial. The resulting charge is then corrected to take into account the cross-talk between calibration lines, leading typically to a few percent increase of the mean total charge for an e.m. shower. The charge is further corrected for eventual dead high voltage layers in some of the periods. Finally a time dependent correction is introduced to take into account a progressive decrease of the signal caused by pollution (outgassing from stack material or leakage from environment). For that, all runs of a given period are scaled to a common early point in time using factors determined by interpolating between 30 GeV "stability" runs taken under identical conditions throughout the period. In all cases, these factors correspond to a decrease of the charge of at most 2 %.

In each period, the charge-to-energy calibration factors were determined first for the e.m. stacks, using electron data, by comparing the measured charge to the expected mean energy deposited (about 3.6 GeV/pC) within the fiducial volume of these stacks. The expected energy deposition was calculated by subtracting from each nominal incident energy the average losses in the beam elements and obstacles in front, as estimated by a detailed GEANT Monte Carlo procedure with very low tracking cuts. These energy dependent corrections represent at most a 0.5 % decrease of the calibration factors. The calibration factors to bring the signal in the hadronic section to an electromagnetic scale were then deduced by extrapolation using Monte Carlo simulations to compare electrons starting directly at the entering plane of the electromagnetic and hadronic sections. Thus, the hadronic/e.m. ratios of the scaling factors were fixed to 2.1 for CBH/CBE and 2.0 for FBH/FBE and IFH/IFE [4]. The e/π separation analysis presented in sections 5.3 and 5.4 are performed at such an electromagnetic scale.

The e or π events are validated by requiring the firing in coincidence of at least 6 PM's of each of the two upstream CEDARs. We furthermore require that there be one and only one hit in each of the MWPC chambers. Finally a minimal threshold of 1 GeV of total calorimeter energy is applied. This cut removes about 1 % of true pions. The list of the datasets considered in the following analysis is given in table 2.

The trigger requirements ensure at 30 GeV an upper limit on the π contamination probability in the e data well below 10^{-4} as could be checked by an unsuccessful search for events with abnormally low e.m. fractions (< 10 %) in the e-tagged data (about 50 % of the π at 30 GeV would satisfy such a cut). A similar figure is expected for the contamination of e in the π-triggered data [7]. In absence of an explicit cross-check, the π-rejection performances of the H1 LAr calorimeter presented in the following sections might nevertheless be considered as lower limits.

5 Analysis and results

5.1 Clustering

We used a simple projective cone algorithm optimized for the measurement of e.m. showers. Taking as a seed the most energetic e.m. or hadronic cell in an octant, the group of 4 hottest contiguous cells (including the seed) is formed. A 6.5° cone is then opened around an axis

Config.	Module	$z^{\mathrm{H1}}_{\mathrm{vtx}}$(cm)	θ	E (GeV)	N_e	N_π
1	**FB1**/FB2	1.8	34.3°	30	11197	38579
				80	1775	1445
				166	$\sim$ 1000	-
2	**CB3**/FB1	2.2	53.5°	5	$\sim$ 3000	-
				10	13254	2838
				20	5957	12997
				30	19360	20499
				40,50	$\sim$ 3500	-
				80	$\sim$ 7000	-
3	**CB2**/CB3	-21.6	79.0°	10	3974	2020
				20	3788	4914
				30	1892	3204
				50	$\sim$ 2500	-
3	CB2/**CB3**	24.2	79.0°	10	3955	1786
				20	4371	3746
				30	10102	15754
				50,80	$\sim$ 2500	-
4	**IF**	-34.1	10.1°	10	1313	1290
				15	$\sim$ 2000	-
				20	1192	1498
				30	2459	1490
				50,166	$\sim$ 3000	-

Table 2: *Run configurations and the corresponding datasets. The e and π's are impinging on the module printed in bold-face. The $z^{\mathrm{H1}}_{\mathrm{vtx}}$ are the mean z value of the point of closest approach to the beam axis in the* H1 *coordinates. The impact angles θ were chosen so that the modules entry face are orthogonal to the impact direction in the $x^{\mathrm{H1}} - y^{\mathrm{H1}}$ plane for configurations* 1 *to* 3. *In configuration* 4, *the entry face is at constant z^{H1}.*

passing through their common energy weighted centroid and the H1 equivalent vertex z^{H1}_{vtx}, starting from a distance of 1 m from the energy centroid (see fig. 3). All cells i having a geometrical centroid within this cone and an energy above $n_\sigma \times \sigma^i_{\mathrm{noise}}$ are kept as member of the cluster, where n_σ is a constant of order 1 and $\sigma^i_{\mathrm{noise}}$ is the energy equivalent of the r.m.s. electronic noise fluctuations in channel (cell) i measured in randomly triggered events. This noise corresponds typically (e.g. on average for CB3 cells) to 20 MeV (40 MeV) for e.m. (hadronic) cells and depends linearly on the cell volume.

The 6.5° **cluster cone** contains what we define as the **electromagnetic shower envelope** which comprises the e.m. cells and the ones of the first hadronic layer. Its opening angle was optimized for electron linearity and resolution performances (see next section). For e/π separation studies, we further consider the leakage in an **isolation cone** starting at z^{H1}_{vtx} with a 15.0° opening angle around the same axis as for the cluster cone. Except if mentioned otherwise, all e/π separation studies were done with an underlying noise cut (in units of $\sigma^i_{\mathrm{noise}}$) of $n_\sigma = 2.5$.

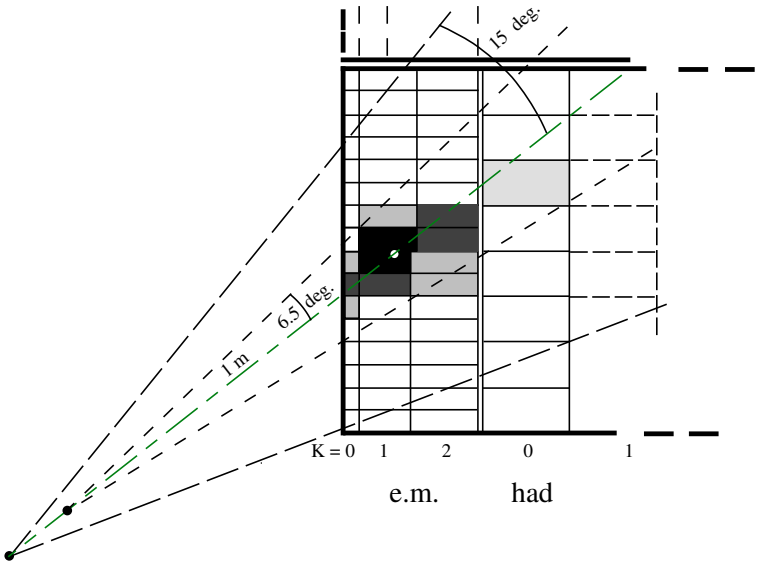

Figure 3: *Ingredients of the projective cone algorithm. The* 6.5° *cone contains the e.m. shower envelope and is surrounded by a* 15.0° *isolation cone which would essentially contain a hadronic shower.*

5.2 Resolutions and linearity

The opening angle of the electron cone and the level n_σ of the noise suppression cuts have to be adjusted to ensure an optimal linearity with stable resolution performances. In the present case, given the quality requirements for deep inelastic scattering physics at HERA collider, a deviation from linearity inferior to 1 % is desired over the energy range from 5 to 166 GeV covered by the CERN test data

The mean collected charge per unit energy measured inside the e.m. shower envelope with the CB3 module of configuration 2 (^{2}CB3) is plotted as a function of incident energy in fig. 4 (a) for noise cuts varying from $n_\sigma = 1.0$ to $n_\sigma = 4.0$ (note the enlarged scale on the y-axis). Given the asymmetric noise cut used in this analysis, the electronic noise adds on average in each channel layer a positive offset to the *physics induced* charge and plays an important role towards lower energies. For low noise cuts (e.g. $n_\sigma = 1.0$) an increasing excess of noise is kept with decreasing energy while on the contrary we suppress an increasing fraction of physics induced signal for a high noise cut (e.g. $n_\sigma = 4.0$).

The calibration factors are found to be only slightly dependent on the opening of the electron cone for a cut $1.5 \leq n_\sigma \leq 2.5$ and for opening angles $5.0° \leq \theta_{\rm cone} \leq 7.0°$. Further increase of the noise cut truncates a significant fraction of the signal for $\theta_{\rm cone} \leq 6.0°$ above 50 GeV. The deviations from linearity for a 6.5° cone in the $n_\sigma = 1.5$ case are shown for all module configurations in fig. 4 (b). In all cases, a deviation from linearity inferior to ± 1 % is achieved. It should be noted however that this excellent linearity partly results from a delicate *cancellation* between the loss in physical signal and the contribution of the noise within the fixed e.m. cluster envelope used here. Another approach using symmetric noise cuts and Monte Carlo extrapolations will be presented in a separate paper where an absolute comparison of the electron calibration factors obtained from the various test configurations will be discussed [3].

The energy resolutions achievable within the electron envelope of the clustering cone for a 6.5° cone and a $n_\sigma = 1.5$ noise cut applied on individual cells are obtained from

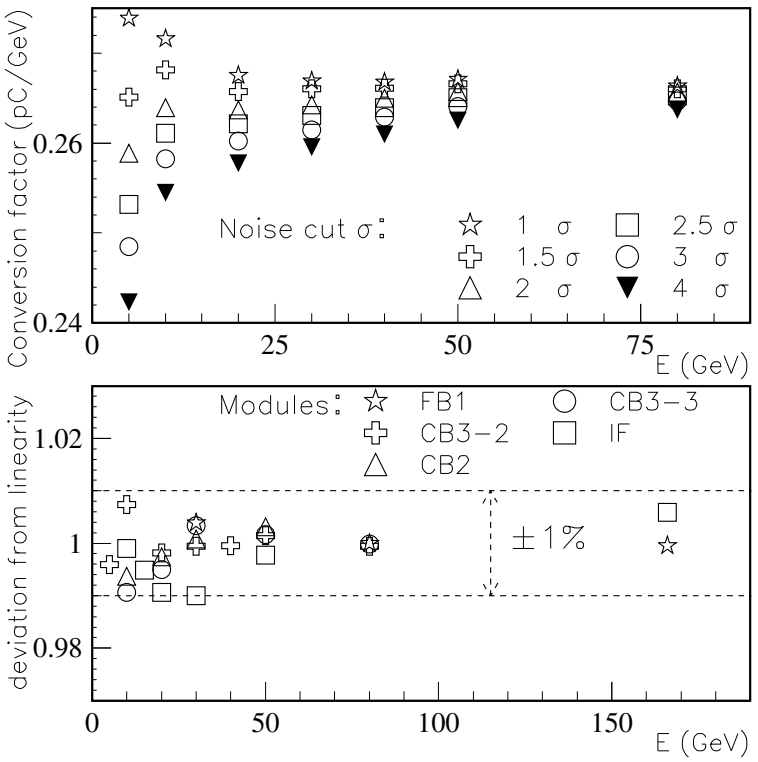

Figure 4: *Linearity performances of the* H1 *LAr modules for electrons measured with a projective cone cluster:* (a) *calibration factors in* ^{2}CB3 *for various noise cuts as function of incident energy;* (b) *deviations from linearity as a function of incident energy in each configuration for a cone opening of* 6.5° *and a* $1.5\,\sigma_{\rm noise}$ *cut.*

Gaussian fits of the total energy distributions. The fits are performed on an asymmetric domain $[\langle Q\rangle - 1.5\,\sigma_{\rm rms}, \langle Q\rangle + 3\,\sigma_{\rm rms}\,]$ in order to be insensitive to the low energy tail in electron data which is specific to the actual test data and is due to straggling in the dead materials along the beam line downstream of the calorimeter modules. This low energy tail is independent of the energy and the test period. In all cases, about 1.7 % of the electrons are found below $\langle Q\rangle - 3\,\sigma_{\rm rms}$ (about 2.9 % below $\langle Q\rangle - 3\,\sigma_{\rm Gauss.}$). The χ^2 per degree of freedom of the Gaussian fits are in all cases excellent and vary between $\sim$ 0.5 and $\sim$ 1.5 with no systematic trend versus energy or period.

The measured resolutions obtained from electron data in each configurations in the energy range from 5 to 166 GeV was fitted with a function:

$$\frac{\sigma(Q)}{Q} = \frac{c_1}{E} \oplus \frac{c_2}{\sqrt{E}} \oplus c_3 = \frac{\sqrt{c_1^2 + c_2^2\,E + c_3^2\,E^2}}{E} \qquad (1)$$

where c_2 represents the contribution from sampling fluctuations, c_1 the noise term and c_3 accounts for systematics and for the dispersion of the incident beam momenta.

The fits are illustrated in fig. 5 in a σ/E vs. $1/\sqrt{E}$ plot for the three test configurations (four modules) where we have data below 30 GeV. The values of the parameters c_1, c_2 and c_3 obtained for each module are given in table 3. The cases where we have the largest number of data points, namely ^{2}CB3 and IF, were first fitted using the function (1) and three free parameters. The weighted mean average of c_3 was then imposed for the fits of CB2 and ^{3}CB3 data. Finally, c_1 and c_3 were imposed when fitting the FB1 data where we considered only three data points. The CB (and FB) data sets give mutually consistent results for

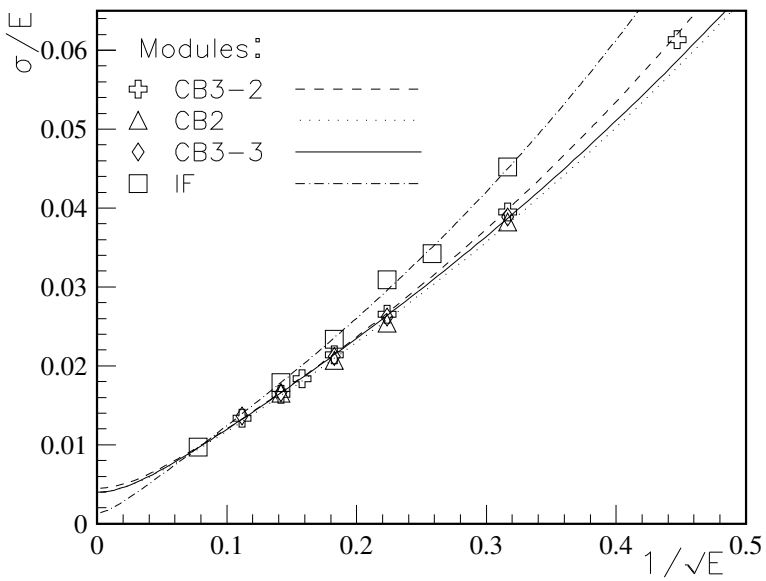

Figure 5: *Fractional charge resolution* σ_Q/Q $(= \sigma_E/E)$ *vs.* $1/\sqrt{E}$ *for electron energies in the range* 5 *to* 166 GeV *for four LAr modules. The data are fitted to the resolution function (1) (see text).*

Table 3: *Results of the resolution function fits. Contributions of the noise term* c_1*, the sampling term* c_2 *and the "constant term"* c_3 *as well as the* χ^2 *per degree of freedom of the fits. All entries having quoted errors were left as free parameters in the fitting procedure.*

Stack	χ^2	c_1 (MeV)	c_2 (%$\sqrt{\text{GeV}}$)	c_3 (%)
FB1	2.6	183	11.6	0.47
			±0.3	
[2]CB3	0.17	188	10.8	0.51
		±15	±0.3	±0.09
CB2	1.07	163	10.8	0.47
		±24	±0.2	
[3]CB3	0.43	163	11.0	0.47
		±21	±0.2	
IFE	1.69	234	12.1	0.16
		±35	±0.4	±0.24

each contribution to the energy resolution. We typically obtain a sampling contribution of $11\% \times \sqrt{\mathrm{GeV}}$ and we are left, at *infinite* energies, with a constant term of 0.5 % which is comparable to the incident beam momentum spread. A larger value of the sampling term c_2 is observed for the IF data which suffered from an additional $0.7 - 0.8\,\mathrm{X_0}$ of dead material in front compared to the CB data. Moreover, there are about twice as many cells in the clustering cone envelope for the IF compared to the CB3 data which explains the larger noise contribution c_1.

5.3 Electron pre-selection within an e.m. shower envelope

We first study the e/π separation performances achievable within the (smallest) optimal volume for electromagnetic shower measurements. Hence we only consider the information from the electron shower envelope within the 6.5° electron cluster cone. Here we restrict to the cells in the e.m. section of that envelope neglecting the small leakage of electromagnetic showers in the hadronic section mostly due to weakly attenuated photons ($\lesssim 1\,\%$ on average for 30 GeV electrons in all configurations). Moreover, we do not assume, for the moment, that we have access to *a priori* information on incident momenta and impact point that could be provided by a tracking detector. These restrictions are motivated by applications in reconstruction algorithms which are often performed on a detector-by-detector basis and where an early (fast) independent tagging of potential electron candidates is desired.

5.3.1 Minimal requirements

We start by applying a set of minimal requirements on the electron and pion data which will be maintained throughout the analysis within the e.m. shower envelope. We ask for at least one firing cell in the first layer ($k = 0$) of the e.m. section (i.e. $E_{k=0}/E_{\mathrm{em}} \neq 0$) and at least one additional cell in the e.m. section within the cluster cone (i.e. $E_{k=0}/E_{\mathrm{em}} \neq 1$). Moreover, in order to get rid of pions punching through the e.m. section, we require that the total energy measured in the e.m. section of the cluster cone satisfies $E_{\mathrm{em}} \geq 1\,\mathrm{GeV}$. Both requirements are satisfied in all module configurations and incident energies considered by 100 % of the electrons. They lead, e.g. at 30 GeV, to π-rejection factors of $R_{e/\pi} = 1.7$ (FB1), 1.9 (^{2}CB3), 2.9 (CB2), 2.1 (^{3}CB3) and 1.7 (IF), where $R_{e/\pi}$ is defined as the ratio $R_{e/\pi} = \epsilon_e/\epsilon_\pi$ of the electron detection efficiency ϵ_e over the probability ϵ_π to misidentify a pion as an electron. These factors vary linearly with incident energy with a slope depending on the module configuration. They improve slightly towards lower incident energies reaching for instance at 10 GeV, 3.2 (CB2), 2.7 (^{3}CB3) and 1.8 (IF).

5.3.2 Global estimators

Within the volume defined by the electron shower envelope, we are interested in peculiarities of the e.m. showers. The ones which distinguish them best from hadronic showers are an early start characteristic of the $\mathrm{X_0}$ scale for electron energy losses by Bremsstrahlung and a compact hot core. Hence we can define simple pre-selection estimators based on the fraction of the e.m. energy which is deposited in the first e.m. layer ($E_{k=0}/E_{\mathrm{em}}$) and the fraction of the energy contained in the "hot" core of the most energetic e.m. group of N contiguous cells which include the hottest cell ($E_{\mathrm{hot}N}/E_{\mathrm{em}}$). The N cells forming the core are allowed to belong to any of the first two e.m. layers ($k = 0$ or 1) for the CB2, CB3 and FB1 modules or to any of the first three layers ($k = 0$, 1 or 2) for the IF module. This ensures in each case that the "core" contains the e.m. showers maxima but remains safely below $1\,\lambda_\mathrm{I}$ in depth. The optimal number N of cells in the core were chosen in each configuration to optimize the e/π

separation and to contain a similar mean fraction of the e.m. showers energy. We use $N = 4$ for CB2, 8 for CB3 and FB1, and 12 for IF such that $E_{\mathrm{hot}N}/E_{\mathrm{em}} \simeq 85 - 90\,\%$ for 30 GeV electrons ($90 - 95\,\%$ for 10 GeV electrons). Typical event densities for these estimators are shown in fig. 6 (a) and (b) for similar initial populations of e and π at 30 GeV (^{2}CB3). The distributions are obtained after imposing the set of minimal requirements of section 5.3.1. The fig. 6 (c) and (d) show correlation plots for electrons and pions respectively.

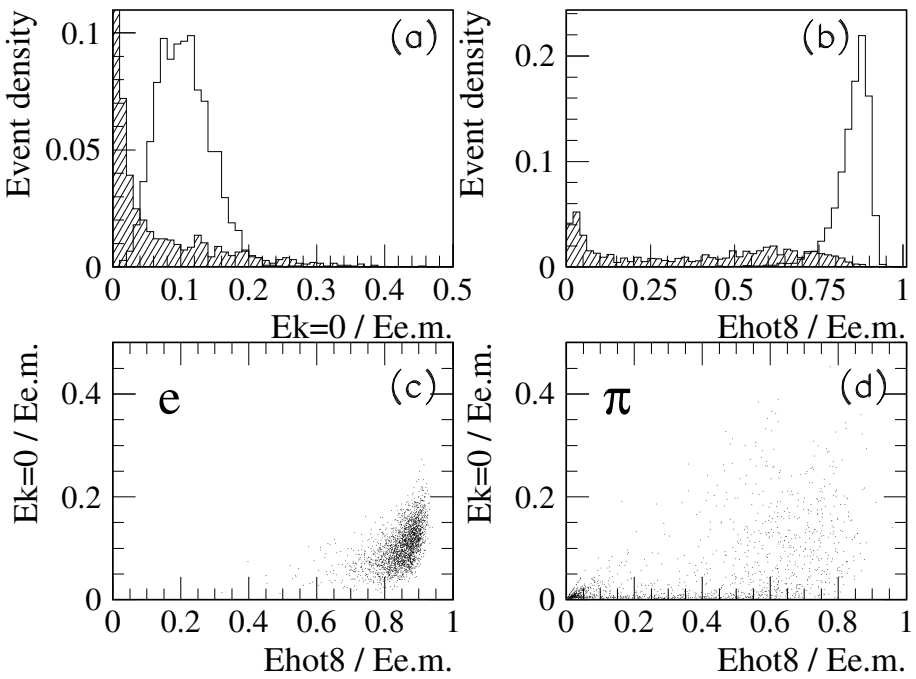

Figure 6: *Event density distributions for the estimators* (a) $E_{k=0}/E_{\mathrm{em}}$ *and* (b) $E_{\mathrm{hot}8}/E_{\mathrm{em}}$ *for* e (opened) *and* π (hatched) *at* 30 GeV *in* ^{2}CB3. *Correlation plots for these two estimators are shown in* (c) *for* e *and* (d) *for* π.

To calculate rejection factors, the estimators are combined on event-by-event via $\vec{x} = (\ln E_{k=0}/E_{\mathrm{em}},\, E_{\mathrm{hot}N}/E_{\mathrm{em}})$ into a χ^2-like estimator making use of the full covariance matrix:

$$\xi^2 = (x - \bar{x})^T \boldsymbol{C}^{-1} (x - \bar{x}) = \sum_{i,j} (x_i - \bar{x}_i) C_{ij}^{-1} (x_j - \bar{x}_j) \qquad (2)$$

where $\bar{x}_i$ as well as the dispersions and correlations entering the calculation of the covariance matrix C are obtained from electron data. From this ξ^2 estimator, we obtain π-rejection factors which are largely independent of energy in the 10 to 80 GeV range. We find for 30 GeV pions at $\epsilon_e = 99\,\%$ that $R_{e/\pi} = 8.0$ (FB1), 7.5 (^{2}CB3), 7.7 (CB2), 10.5 (^{3}CB3) and 25.4 (IF). The best rejection factors are obtained for IF which is the most finely segmented module and for which on event-by-event, the $N = 12$ cells of the $E_{\mathrm{hot}N}/E_{\mathrm{em}}$ better match the true core of the e.m. showers.

5.3.3 Longitudinal shower shape

Given an approximate shower direction (taken for the moment as the axis passing through the mean cluster centroid and the mean H1 equivalent vertex), we can make use of the

a priori knowledge on the expected longitudinal shower shape under the electron hypothesis. In practice, this amounts, given a shower energy E measured in the electron envelope and distributed among cell layers, to calculate iteratively the parameters of a function describing the dE/dl shower shape and compare the obtained values with those expected for electrons at an incident energy of $E_{\rm inc} = E$.

When integrating over coarse enough layers, i.e. $\Delta L \gg 1\,{\rm X}_0$, the mean longitudinal development of an e.m. shower is well described by the Longo-Sestilli empirical formula [10]:

$$\frac{dE}{dl} = E_{\rm inc}\,\frac{\beta^\alpha}{\Gamma(\alpha)}\,l^{\alpha-1}\,e^{-\beta l} \tag{3}$$

where l is the shower depth in units of $\rm X_0$ and α and β are energy dependent free parameters. This is seen for example on fig. 7 for which the profile formula (3) (integrated over each layer) was fitted, using $a = 1/\alpha$ and $b = \beta/\alpha$ as free parameters, to the average energy measured in the three e.m. layers of ^{3}CB3 for electrons of $E_{\rm inc} = 10$, 20 and 30 GeV. We

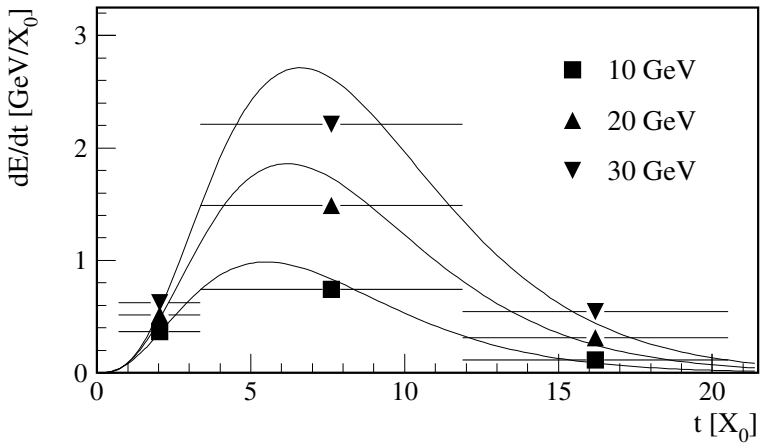

Figure 7: *Fits of the mean longitudinal shower energy density (per* $\rm X_0$ *unit) profiles measured in the three e.m. layers of the* ^{3}CB3 *module for e at* 10, 20 *and* 30 GeV.

obtain consistent values of the fit parameters at a given energy for different modules and impact angles. Averaging out the fit values (compatible within errors) found for ^{2}CB3 and ^{3}CB3, we obtain for example that $a = 1/\alpha = 0.263$, 0.243, 0.232 ($\pm$0.001) and $b = \beta/\alpha = 0.134$, 0.122, 0.116 ($\pm$0.001) for electrons of 10, 20 and 30 GeV respectively. This is in excellent agreement with the empirical formulae [11] of

$$\alpha \simeq \left(0.492 + \frac{2.38}{Z_{\rm eff}}\right) \ln \frac{E_{\rm inc}}{\epsilon_{\rm c}} \tag{4}$$

and

$$\beta = \frac{\alpha - 1}{\ln \frac{E_{\rm inc}}{\epsilon_{\rm c}} - 1.3} \tag{5}$$

which were derived from a detailed GEANT simulation and for which the critical energy $\epsilon_{\rm c}$ was given in table 1 and the effective Z of the media in the e.m. section is $Z_{\rm eff} \simeq 66.8$. Such formulae are used for the parametrization of e.m. showers in the fast simulation programs of H1.

The parameters a and b are related in a simple way to the first and second order moments of the shower:

$$b = \frac{1}{\langle l \rangle} \quad , \quad a = \frac{\langle l^2 \rangle - \langle l \rangle^2}{\langle l \rangle^2} \tag{6}$$

The equations (3) and (6) can be used as a basis for an iterative procedure to determine a and b on an event-by-event basis. We use the energy weighted first ($m = 1$) and second ($m = 2$) moments calculated over 3 layers (4 in the case of IFE data) as $\langle l^m \rangle = (\sum_{k=1}^{3} E_k l_k^m)/\sum_{k=1}^{3} E_k$. At first iteration, the depth l_k is given by the geometrical centroid of layer k. The a and b are then deduced from eq. (6) and injected into eq. (3). In subsequent iterations, the l_k^m are evaluated taking into account the distribution of energy *within* layer k according to this shower profile shape, i.e.

$$l_k^m = \int_k l^m \frac{dE}{dl}(a,b)dl / \int_k \frac{dE}{dl} dl \,.$$

Updated values of a and b are calculated from the resulting shower moments using (6) and these parameters are in turn injected back into (3), and so on. After three iterations we obtain stable values of a and b (this is strictly true for electrons while for pions the procedure converges about half of the time). These are largely uncorrelated and Gaussian distributed for e.m. showers but rather flat for hadronic showers as seen in fig. 8 (a) and (b). Making use

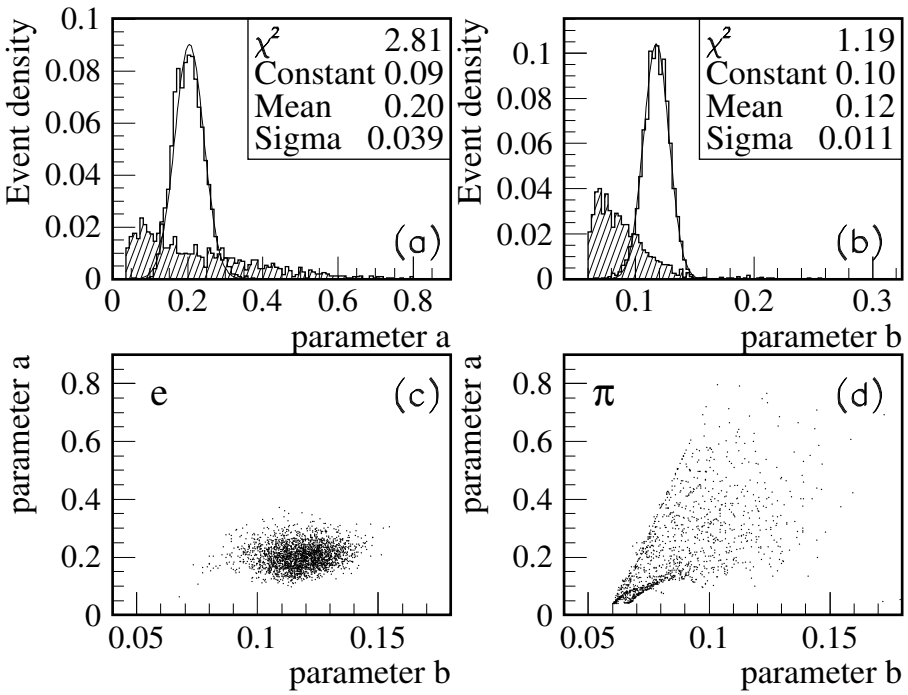

Figure 8: a,b) *Event densities for the parameters a and b of the longitudinal shower shape for e (opened) and π (hatched). The e distributions are fitted to Gaussian functions. Correlation plots for these two parameters are shown in* (c) *for e and* (d) *for π.*

of the *a priori* knowledge of the mean a and b values and their dispersions as parametrized with energy using electron data, we can then build a χ^2_{ab}. From that shower shape estimator, we obtain (fig. 9 (a)) similar rejection factors in all configurations, with values in the range $R_{e/\pi} \sim 5.5$ to 7.5 for energies in the range 10 to 30 GeV. The obtainable π-rejection further improves when rising the noise cut. This is seen for example in fig. 9 (b) in the case ^{3}CB3 where $R_{e/\pi}$ improves from $\sim$ 6.3 at $n_\sigma = 2.5$ to 10.6, 9.2 and 8.2 for $E_{\rm inc} = 10$, 20 and 30 GeV respectively at $n_\sigma = 8$. The a and b parameters for π are sensitive to the rise of the noise cut which mostly truncates peripheral cells in their shower expansion while the process leaves e shower parameters unaffected. Hence the χ^2_{ab} allows for (noise-dependent) π-rejection factors comparable to those obtained with the global estimators of section 5.3.2.

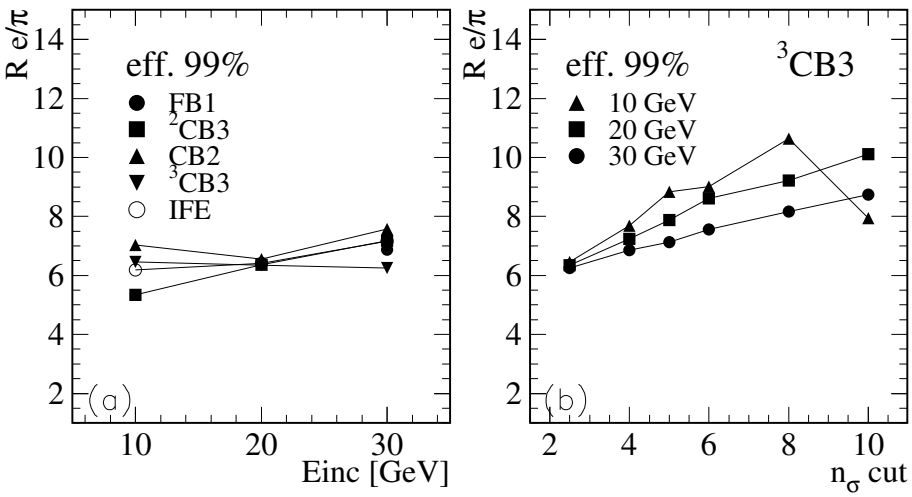

Figure 9: *Rejection factors $R_{e/\pi}$ for $\epsilon_e = 99\,\%$ obtained with the χ^2_{ab} estimator* (a) *vs. energy for all module configurations and* (b) *vs. the noise cut for* CB3 *in configuration 3.*

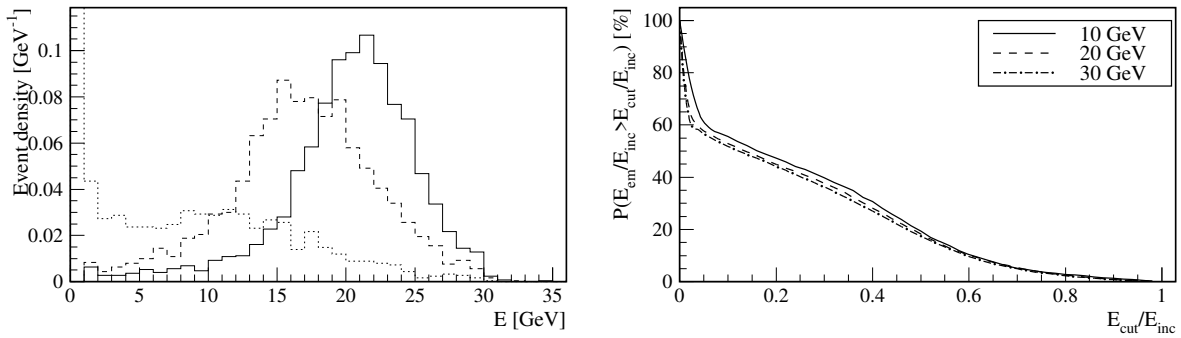

Figure 10: (a) *Distribution of the energies measured in the electron e.m. envelope* (dotted), *the cluster cone* (dashed) *and the isolation cone* (solid) *for* 30 GeV π^+ *and* (b) *hadronic opaqueness for* 10, 20 *and* 30 GeV π^+, *in* ^{2}CB3 *data.*

5.3.4 Hadronic opaqueness

The energy measurement restricted to the smallest volume containing the e.m. shower is optimal for performing e/π separation by the matching with an independent momentum estimator provided by a tracking detector. As can be seen for instance on fig. 10 (a) for 30 GeV pions at the e.m. calibration scale, the electron envelope is largely transparent to hadrons. We define a measure of the non-transparency (opaqueness) as the probability that the fraction of the π incident energy $E_{\rm inc}$ recovered in the e.m. section within the 6.5° cone be above a threshold fraction $E_{\rm cut}/E_{\rm inc}$. This measure of the pion suppression power is shown in fig. 10 (b) for 10, 20 and 30 GeV pions impinging on CB3.

The electron envelope (hence the LAr e.m. section) is seen to be almost as transparent at 10 GeV than at higher π energies. This can be understood given the fact that the fraction of the incident π^+ energy transferred to π^0's by the chain of inelastic interactions in the shower increases (logarithmically) with energy while the interaction length stays rather constant in the energy range considered.

5.4 Electron identification within the isolation cone

We now consider the electron identification performances using calorimetric information from the full isolation cone. This is particularly relevant in the context of H1 at HERA where the physics imposes the application of an isolation criterion for the scattered electron from deep inelastic collisions.

5.4.1 Global properties and longitudinal sampling

In the full isolation cone, we consider four pre-selectors. We again make use of the simple global properties introduced in section 5.3.2, namely the fraction of e.m. energy deposited in the first e.m. layer ($E_{k=0}/E_{\rm em}$) and the fraction contained in the hot core of the most energetic e.m. group of N contiguous cells ($E_{{\rm hot}N}/E_{\rm em}$). These can now be complemented by a powerful estimator relying on the longitudinal leakage of π showers in the hadronic section ($E_{\rm em}/E_{\rm tot}$) and by the fraction of energy leaking out transversely from the clustering cone within the "isolation" cone ($(E_{\rm iso}-E_{\rm tot})/E_{\rm tot}$); both of these being normalized to the total energy $E_{\rm tot}$ in the full 6.5° clustering cone (i.e. including cells of the hadronic sections). Typical event densities for these last two pre-selectors relying on properties of the hadronic shower expansion are shown in fig. 11 (a) and (b). It should be noted that for π showers with large values of $E_{\rm em}/E_{\rm tot}$, this e.m. fraction is only weakly correlated with $E_{{\rm hot}N}/E_{\rm em}$.

It is interesting to study how the e.m. fraction estimator $E_{\rm em}/E_{\rm tot}$ can be, by itself, optimized by adjusting the thickness (in X_0 or $\lambda_{\rm I}$) of the e.m. section. For that, we can profit from the longitudinal segmentation of the modules and particle penetration angles in order to vary the effective "e.m. section" length L over which $E_{\rm em}$ is integrated (notwithstanding the fact that the cell layer planes are actually not perpendicular to the impact directions). The rejection factors obtained at fixed ϵ_e as a function of L are shown at 10, 20 and 30 GeV in fig. 12 which cumulates the data of the various configurations. The optimal L can be seen to slightly increase with energy with a maximum around $L \approx \lambda_{\rm I}$. The worse rejections are obtained for $L \approx 6\,X_0$, i.e. with an e.m. section ending around the e.m. shower maximum.

In order to calculate the rejection factors provided by a combination of parallel cuts on the four pre-selection estimators introduced above, we take into account the energy dependence of the cuts. This is necessary because we are interested in the rejection power for a π of a certain energy to be misidentified as an electron of *any* energy. The rejection factors obtained as a function of incident π energy from a combination of global properties within the isolation cone are shown in fig. 13 (a). A simple energy dependent combination of cuts on $E_{k=0}/E_{\rm em}$, $E_{{\rm hot}N}/E_{\rm em}$, $E_{\rm em}/E_{\rm tot}$ and $(E_{\rm iso}-E_{\rm tot})/E_{\rm tot}$ gives rejections rising from 0.5 to 1.1×10^2 at 10 GeV up to 0.9 to 3.1×10^2 at 30 GeV for $\epsilon_e = 97\,\%$. Comparable results are obtained when first combining $\ln(E_{k=0}/E_{\rm tot})$ and $E_{{\rm hot}N}/E_{\rm em}$ in a ξ^2-like estimator as in eq. (2) (section 5.3.2). As trivially expected, the π's surviving the preselection cuts have a measured energy approaching that of electrons of the same incident energy. This can be seen on fig. 13 (b).

5.4.2 Impact point matching

The impact point of the incident particles can be reconstructed as the "center-of-gravity" of the energy shared among calorimeter cells, which we take here as $u = (\sum u_i\sqrt{E_i})/\sum\sqrt{E_i}$ with $u = (x,y,z)$. For a single particle this centroid should match with the expected impact provided by an independent tracking detector. This impact point matching, which is generally limited by the quality of the position resolution for e.m. showers, is a powerful method to suppress overlap (e.g. $\gamma\pi^{\pm}$) contamination in single particle tagging. The position

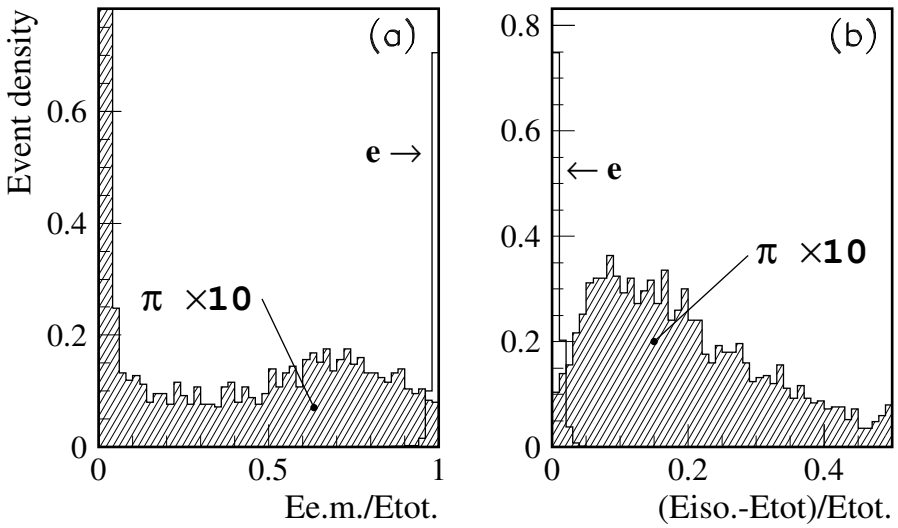

Figure 11: *Event density distributions for* e (opened) *and* π (hatched) *at* 30 GeV *in* ^{3}CB3 *for the estimators:* (a) $E_{\rm em}/E_{\rm tot}$ *and* (b) $(E_{\rm iso} - E_{\rm tot})/E_{\rm tot}$.

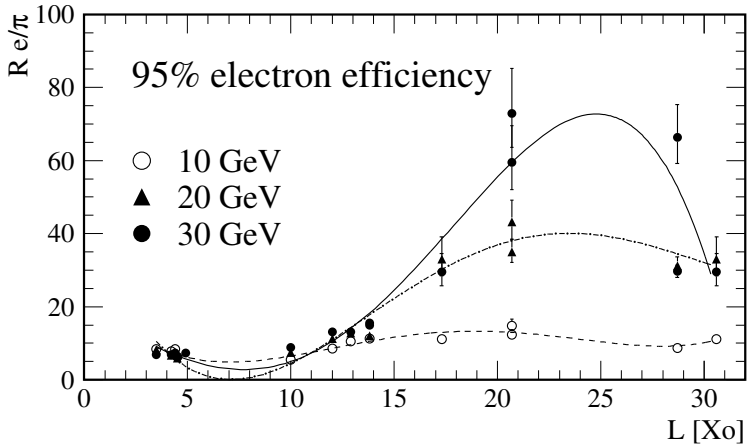

Figure 12: π*-rejection factors from longitudinal sampling vs. the e.m. section length* L *obtained at* $E_{\rm inc} = 10, 20$ *and* 30 GeV *for* $\epsilon_e = 95\,\%$.

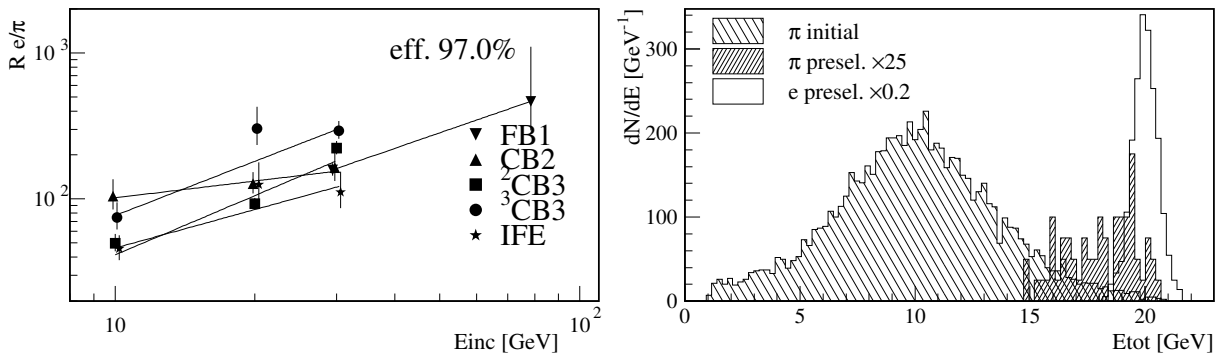

Figure 13: (a) π*-rejection factors from simple energy dependent cuts on four pre-selectors (see text) for all configurations and energies at* $\epsilon_e = 97\,\%$. (b) *The initial energy distribution (within the cluster cone) of pions* (hatched) *shrinks after preselection* (dark $\times 25$) *approaching the electron one* (opened $\times 0.2$).

resolution of our various H1 LAr modules can be derived from CERN data by comparison with the impact point provided by the MWPCs.

From the last MWPC which provides an impact resolution of $\sigma \simeq 2\,\mathrm{mm}/\sqrt{12}$ in both horizontal (x_I) and vertical (y_I) directions, the beam particles have essentially parallel trajectories and, hence, the constant impact angles given in table 2 in the H1 coordinates. A displacement in (x_I, y_I) can be translated on event-by-event into a displacement of the H1 equivalent vertex (i.e. the point at the distance of closest approach to the z^{H1} axis) from the mean values given in table 2. The θ and ϕ angles sustained by the energy centroids viewed from such vertices can then be compared to the nominal impact angles. The deviations are shown for example in fig. 14 (a) and (b) as a function of the MWPC coordinates of impact for 30 GeV e in ^{3}CB3. The systematic trends and extrema (e.g. in fig. 14 (b)) are due to the

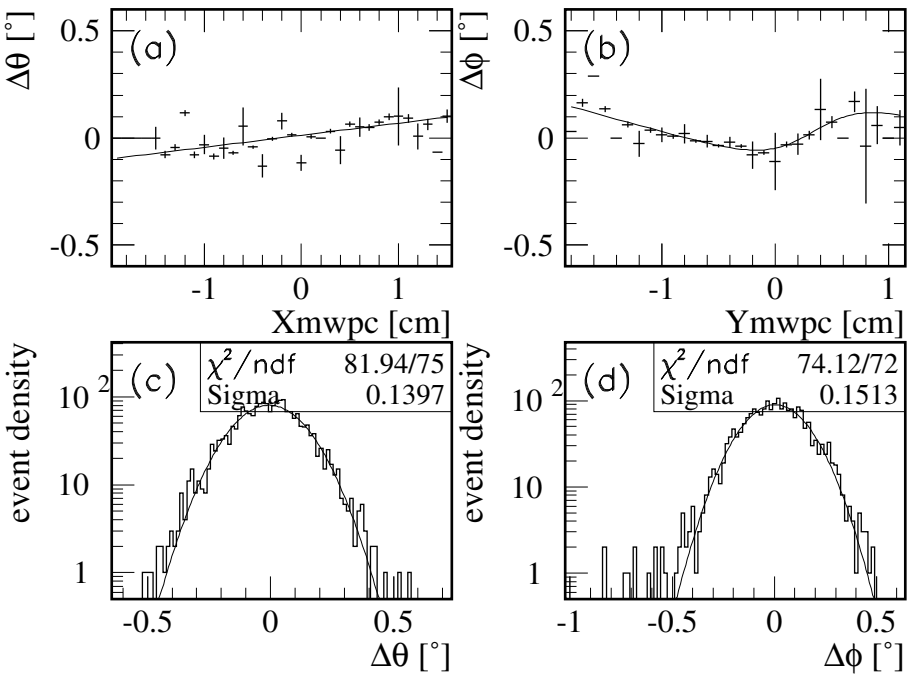

Figure 14: *Deviations of the reconstructed angles* (a) θ *and* (b) ϕ *from the nominal values as a function of the* MWPC *impact point; and angular dispersions from mean values in* (c) θ *and* (d) ϕ *fitted to Gaussian functions, for* ^{3}CB3 *data.*

finite cell sizes and non-projectivity of their lateral boundaries. For this and for other configurations the dependence of the mean deviations on the impact can be simply parametrized and factored out. The remaining angular dispersions in θ and ϕ are Gaussian distributed as shown for example in fig. 14 (c) and (d) for the ^{3}CB3 data.

The variation with incident energy of the spatial resolutions along θ, $u_\theta = D \times \tan\sigma_\theta$, and ϕ, $v_\phi = R \times \tan\sigma_\phi$, are plotted in fig. 15 (a) and (b) respectively. D and R are the mean distances and radii (see caption of fig. 15) from the vertices to the modules front faces. These resolutions are seen to nicely scale in proportion to $1/\ln E$ and are found on average to vary from $\sigma(u_\theta) \simeq 0.37$ to 0.21 cm, and $\sigma(v_\phi) \simeq 0.40$ to 0.23 cm for energies ranging from 10 to 80 GeV. It should be noted that the incident beam profile here only scans a small fraction of a typical cell surface and that the spatial resolution for a given module depends on the impact point (as may be inferred for instance from the varying slope in fig. 14 (b)). Hence the differences between configurations in fig. 15 cannot be generalized as representing average performances of the corresponding modules.

Besides the application in overlap separation, the precision on the impact point reconstruction allows for a separation of single electrons and pions as was noted in [12]. This has to do both with the differences in the scale of the lateral dispersions and with the fact that hadronic showers are less uniformly spread around the principal axis. The θ versus ϕ angular dispersions are shown for example in fig. 16 (a) and (b) for 30 GeV e and π's in the ^{3}CB3 and the resulting deviation $\Delta\psi = \sqrt{(\Delta u_\theta)^2 + (\Delta v_\phi)^2}$ from the nominal impact is shown in fig. 16 (c). This $\Delta\psi$ can be used as an estimator for the e/π separation but its power diminishes as soon as one imposes in parallel a large e.m. fraction of energy $f_{\rm em}$ in the π showers via pre-selection requirements. Since the fraction $f_{\rm em}$ of the π shower energy which is deposited via π^0 components increases on average logarithmically with energy, we expect $\Delta\psi \ln E_{\rm inc}$ to scale linearly with $f_{\rm em}$ and to be roughly independent of $E_{\rm inc}$ at a given $f_{\rm em}$. This is seen to be the case in fig. 17 (a) where the ratio $E_{\rm em}/E_{\rm tot}$ is used as an estimate of $f_{\rm em}$. The angular dispersion approaches that of electrons at large values of that ratio.

The gain in rejection factors when applying a cut on this angular dispersion $\Delta\psi$ on top of the requirement on the e.m. fraction $E_{\rm em}/E_{\rm tot}$ is shown in fig. 17 (b) as a function of a threshold cut on $E_{\rm em}/E_{\rm tot}$. An improvement of the π-rejection of ≈ 1.6 is even obtainable for $E_{\rm em}/E_{\rm tot} > 0.75$.

5.4.3 Separation from a minimal spanning tree

A measure of the characteristic topological patterns of e.m. and hadronic showers can be derived from a non-classical minimal spanning tree (MST) algorithm first borrowed from graph theory by the CHARM II Collaboration [13]. Here the spanning tree can be viewed as a multi-dimensional graph built up progressively by linking calorimeter cells. The links are weighted by a topological distance in a given metric and the MST is that tree which minimizes the total weight (i.e. length) taken as the scalar sum of weights over all links. The tree can be developed starting from an arbitrary seed which we choose to be the hottest cell in the shower. Then the closest cell, according to the chosen metric, is linked and one iterates from there on, always adding the next closest cell to the growing tree until completion, i.e. until $N_{\rm links} = N_{\rm cells} - 1$. One MST solution is thus obtained. Its total weight does not depend on the specific order in which the cells and links were examined.

The choice of the distance weights fixes determines MST building process. We consider the generalized distance between two cells

$$d_k = \sqrt{(c_G d_G)^2 - (c_E d_E)^2} \tag{7}$$

where d_G is a spatial measurement and d_E an energy density measurement with

$$d_G = \sqrt{(3 - 2w_r^2)(\Delta l)^2 + (w_r)^2(\Delta r)^2} \tag{8}$$

where $w_r^2 = 3s^2/(2s^2 + 1)$, and

$$d_E = \sqrt{3}\Delta\rho / N_{cell}\bar{\rho} \tag{9}$$

The c_G and c_E in eq. (7) as well as w_r in eq. (8) are scaling factors. The differences Δl and Δr are measured longitudinally and transversely relative to the cluster principal axis. The distance d_G corresponds to an Euclidian distance if the dilatation factor s is set to 1. The $\Delta\rho$ in eq. (9) is given by $\Delta\rho = (E_i/V_i - E_j/V_j)$ where $E_{i,j}$ and $V_{i,j}$ are the measured energies and volumes of cells i, j and $\bar{\rho}$ is the mean cell energy density.

Having built the MST, we consider as e/π estimators the total weight (length) of the tree $\mathcal{L}_{\rm tot} = \sum_{\rm links} d_k$, and the mean length of the links, $\Lambda = \mathcal{L}_{\rm tot}/N_{\rm links}$. We start by tuning

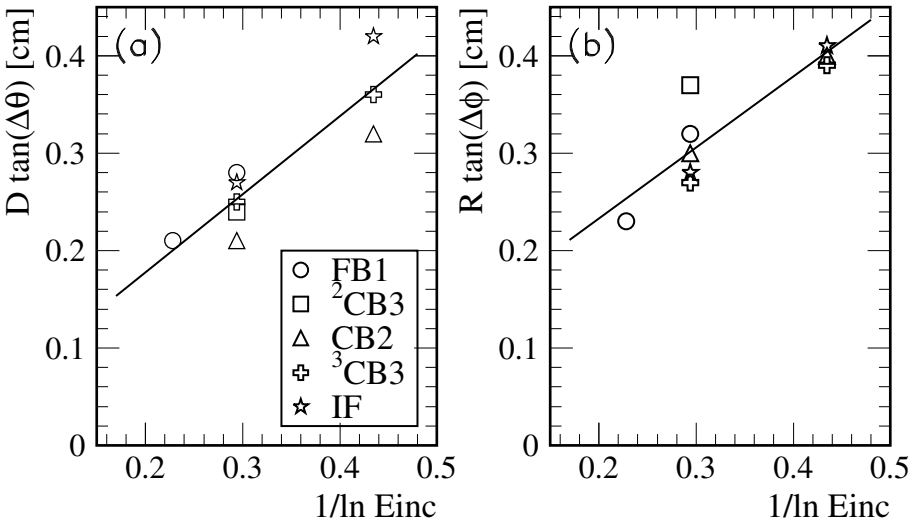

Figure 15: *Spatial resolutions* (a) $D \times \tan\sigma_\theta$ *and* (b) $R \times \tan\sigma_\phi$ *as a function of* $1/\ln E_{\rm inc}$. *The distances* D *are* 178.2 (FB1), 124.9 (^{2}CB3), 102.3 (CB2, ^{3}CB3) *and* 331.2 cm (IF). *The radii* R *are* 59.0 cm (IF) *and* 100.4 cm *in all other cases.*

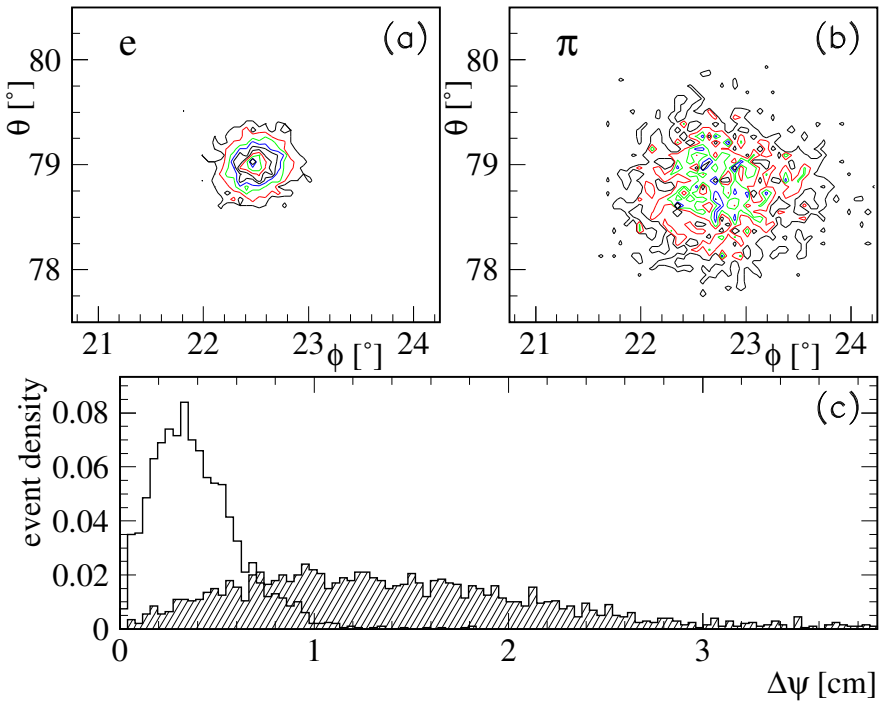

Figure 16: *Impact reconstruction in azimuthal* (θ) *and radial* (ϕ) *angles of* (a) e *and* (b) π *at* 30 GeV *in* ^{3}CB3. (c) *Frequency distributions for the distance deviation* $\Delta\psi$ *relative to the axis for* e (opened) *and for* π (hatched).

a pure geometrical MST by setting $c_E = 0.0$ and vary the transverse dilatation s as well as the noise cut n_σ applied on individual cells. The noise cut affects the overall topology, and hence $\mathcal{L}_{\rm tot}$ since it tends to suppress peripheral cells. The best π rejection is obtained for $s = 5.0$ and $n_\sigma = 7.5$. The corresponding $\mathcal{L}_{\rm tot}$ and Λ measured for 30 GeV e and π's in the ^{2}CB3 period are shown in fig. 18 (a), (b) and (c). Fixed values of N_{links} lead to a clusterisation along diagonal lines in fig. 18 (a). Both $\mathcal{L}_{\rm tot}$ and Λ are Gaussian distributed for electrons and largely independent for pions.

The $\mathcal{L}_{\rm tot}$ and Λ estimators can be combined on event-by-event into a ξ^2 estimator as in eq. (2) with $\vec{x} = (\mathcal{L}_{\rm tot}, \Lambda)$. The π-rejection factors obtained for $s = 5.$ at 30 GeV when comparing pions to electrons of the same incident energy are shown in fig. 18 (d) for a fixed noise cut $n_\sigma = 2.5$ with $c_E = 0.0, 5.0$ or 10.0, and for $c_E = 0.0$ with $n_\sigma = 2.5, 7.5$ and 10.0.

In the case of a purely geometrical tree (i.e. $c_E = 0.0$) with $s = 5.0$ and $n_\sigma = 2.5$, we obtain $R_{e/\pi} \simeq 15$ at $\epsilon_e = 97\,\%$. This improves to $R_{e/\pi} \simeq 25$ when introducing an energy component $c_E = 5.0$. Alternatively, it improves even more when rising the noise cut to $n_\sigma = 7.5$ which leads to $R_{e/\pi} \simeq 95$.

In order to compare our MST results with those of [13], we can exploit the distribution of the weights (lengths) d_k of the links. We consider the frequency ρ_i of links having weights within one of three possible bins ($1.0 \leq d_1 < 2.0 \leq d_2 < 3.0 \leq d_3$) for showers having a given number N_{links}. The ratio ρ_i^e/ρ_i^π for e and π's is shown for each bin as a function of N_{links} in fig. 19 (a). This information can be used on event-by-event basis to define a function

$$F(\alpha) = \sum_{i=1}^{2} \left(\frac{\rho_i - [\alpha \rho_i^e(N_{\rm links}) + (1-\alpha)\rho_i^\pi(N_{\rm links})]}{\sigma_i^e(N_{\rm links})} \right)^2 \qquad (10)$$

that can be minimized as a function of α. Setting $\alpha = 1$, this reduces to the calculation of a χ^2 (with 2 degrees of freedom) which performs the comparison of the measured ρ_i to those expected for electrons. The event densities for the α which minimizes the function $F(\alpha)$ of eq. (10) (an exactly solvable problem) is shown for 30 GeV ^{2}CB3 data in fig. 19 (b). These compare very well with similar plots in [13] and a combined cut on χ^2 and α typically lead to π-misidentification probabilities at the few percent level for $\epsilon_e = 97\,\%$. In that respect, the MST method does not favorably compete with the combination of pre-selection estimators introduced in section 5.4.1.

5.4.4 Shower moments and combined rejection factors

The fine granularity of the H1 LAr calorimeter offers the possibility to use both the longitudinal and lateral shower moments together with their correlations. We consider the first and second order moments calculated relative to the shower principal axis starting from it's intersection with the entry plane of the calorimeter active volume. The moments are elements of the vector $\vec{x}$:

$$\begin{aligned} x(1) &= \langle \ell \rangle & x(3) &= \langle r \rangle \\ x(2) &= \sqrt{\langle \ell^2 \rangle - \langle \ell \rangle^2} & x(4) &= \sqrt{\langle r^2 \rangle - \langle r \rangle^2} \end{aligned}$$

$$x(5) = \langle r\ell \rangle - \langle r \rangle \langle \ell \rangle$$

where $\langle l^n r^m \rangle = (1/\rho) \sum_{cell} \rho_i l_i^n r_i^m$ with the energy densities $\rho_i = (E_i/V_i)$ and $\rho = \sum \rho_i$. These moments are shown in fig. 20 for 30 GeV e and π's of the ^{2}CB3 period. The moments have roughly Gaussian distributions for electrons. The much larger spread of the π distributions

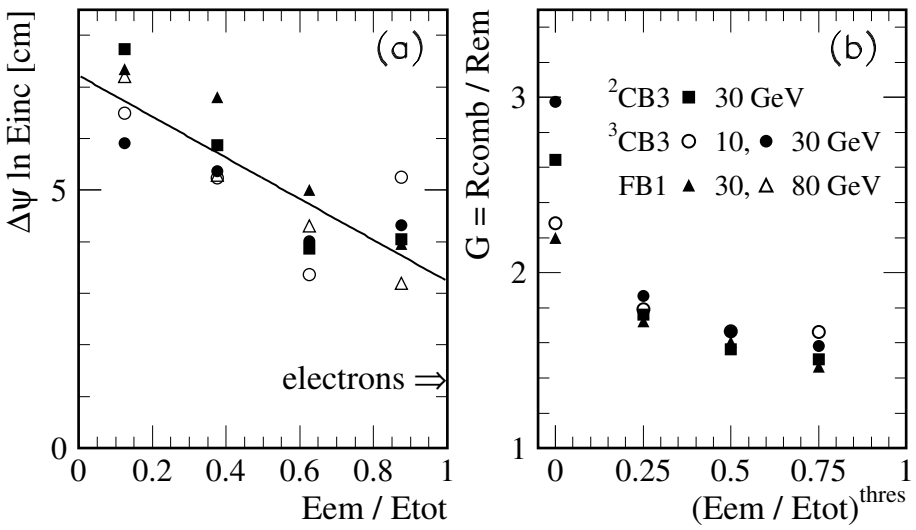

Figure 17: (a) *Scaled distance deviation* $\Delta\psi \times \ln E_{\rm inc}$ *as a function of the mean* $E_{\rm em}/E_{\rm tot}$ *for* π *in various configurations at three incident energies.* (b) *Gain* $G = R_{\rm comb}/R_{\rm em}$ *in the rejection* $(R_{\rm comb})$ *obtained with a combined cut on* $\Delta\psi$ *and* $E_{\rm em}/E_{\rm tot}$ *compared to the rejection* $(R_{\rm em})$ *for a cut on* $E_{\rm em}/E_{\rm tot}$*, as function of a minimal requirement on* $E_{\rm em}/E_{\rm tot}$*.*

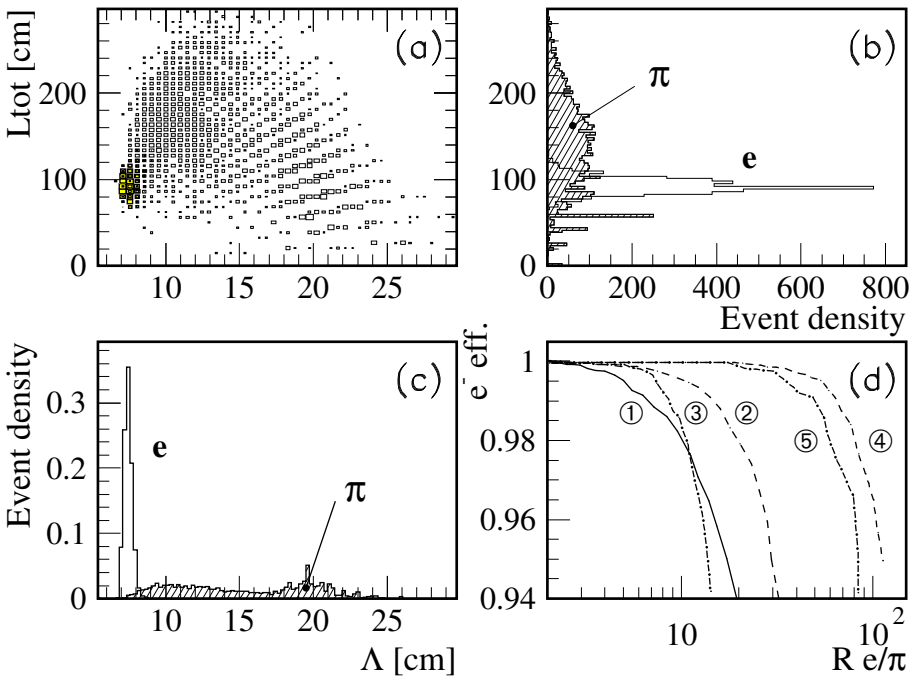

Figure 18: (a) *The MST total length* $\mathcal{L}_{\rm tot}$ *vs. the mean length* Λ *for* 30 GeV *e (closed boxes) and* π *(open boxes) in* ^{2}CB3 *and the projections on* (b) $\mathcal{L}_{\rm tot}$ *and* (c) Λ *obtained for* $s = 5.0$ *and* $n_\sigma = 7.5$*.* (d) ϵ_e *vs.* $R_{e/\pi}$ *for* $s = 5.0$ *and* $n_\sigma = 2.5$ *with* (1) $c_E = 0.$, (2) $c_E = 5.0$ *or* (3) $c_E = 10.0$*; ditto for* $s = 5.0$ *and* $c_E = 0.$ *with* (4) $n_\sigma = 7.5$ *or* (5) $n_\sigma = 10.$

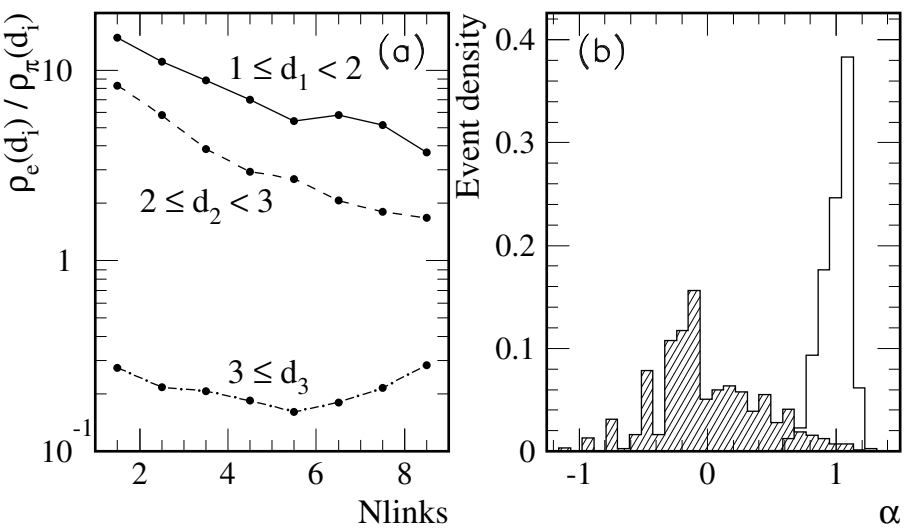

Figure 19: (a) *Ratio $\rho_e(d_i)/\rho_\pi(d_i)$ of the frequency of links of three different classes i for e and π, as a function of the total number of links for a noise cut $n_\sigma = 7.5$;* (b) *distribution of the "electromagneticity parameter" α for e* (opened) *and π* (hatched) *at* 30 GeV *in* ^{2}CB3.

reflects the differences between the electromagnetic (X_0 and R_m) and hadronic (λ_I) scales. Weighting by energy densities (instead of energy) renders the moments less sensitive to noise and enhances the relative contribution of the first e.m. layers. Distributions similar to those of fig. 20 are obtained with energy weighting when rising the noise cut from the default $n_\sigma = 2.5$ to $n_\sigma \approx 7.5$.

For the calculation of π-rejection factors, we consider a combination of cuts on the pre-selection estimators introduced in section 5.4.1 with a ξ^2 exploiting the full 5×5 covariance matrix of shower moments, following the recipe described in eq. (2). Similar ξ^2 estimators, but relying on huge matrices involving as many elements as calorimeter cells, were introduced for e/π discrimination by [14, 15] and used by the D0 Collaboration for their Uranium/LAr calorimeter [16]. The averages and dispersions of the shower moments as well as all other ingredients of the covariance matrix must first be parametrized as a function of electron energy. Obviously, the cuts relevant for an incident π of a certain measured energy E^π are those of an electron of incident energy $E^e_{\rm inc} = E^\pi$. All parameters are found to vary slowly with energy and can be parametrized as a linear function of $\ln E^e_{\rm inc}$. After pre-selection, the correlations between "pure" longitudinal (i.e. $x(1)$ or $x(2)$) and "pure" transversal (i.e. $x(3)$ or $x(4)$) components of $\vec{x}$ are rather weak with linear correlation coefficients within ± 0.2. Applying a Pearson's test to the density distribution of the ξ^2 estimator for electrons, we find as expected that it is compatible with a χ^2 distribution with ~ 5 (i.e. the rank of the covariance matrix) degrees of freedom.

The variation of the π-rejection factors as function of the ϵ_e are shown in fig. 21 (a) for 10, 20 and 30 GeV π's in ^{2}CB3. The rejection factors finally obtained at $\epsilon_e = 95\,\%$ for the full combination pre-selection plus shower moments estimators are shown in fig. 21 (b). The rejections obtained, which rise from $\approx 10^2$ at 10 GeV to $\approx 10^3$ at 80 GeV, are compatible with those obtained by D0 [16] and, for equivalent cell granularity, by Engelmann et al. [15]. Similar shower moment analysis of some of the H1 CERN data sets were discussed in [5, 11, 17] reproducing with good agreement the results presented here. The π-rejection that would be obtained in absence of any transversal segmentation of our modules can be studied here by using only the longitudinal pre-selectors (i.e. $E_{k=0}/E_{\rm em}$ and $E_{\rm em}/E_{\rm tot}$) and the

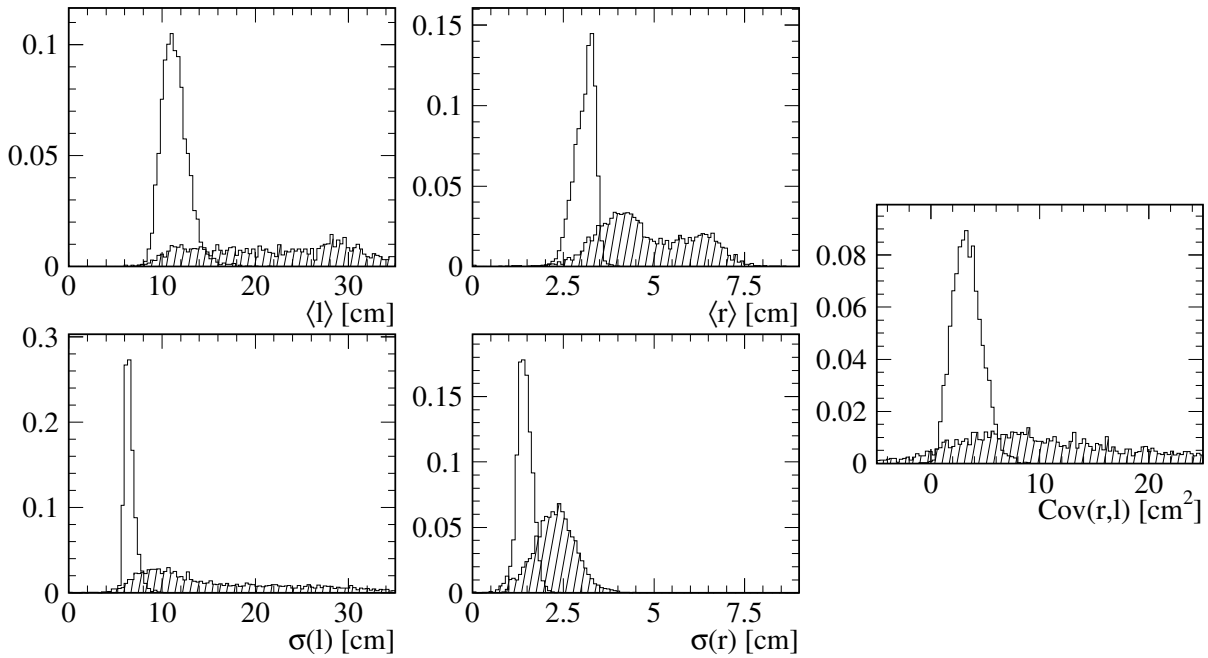

Figure 20: *Shower moment distributions for* e (opened) *and* π (hatched) *measured with the* ^{2}CB3 *module at* 30 GeV.

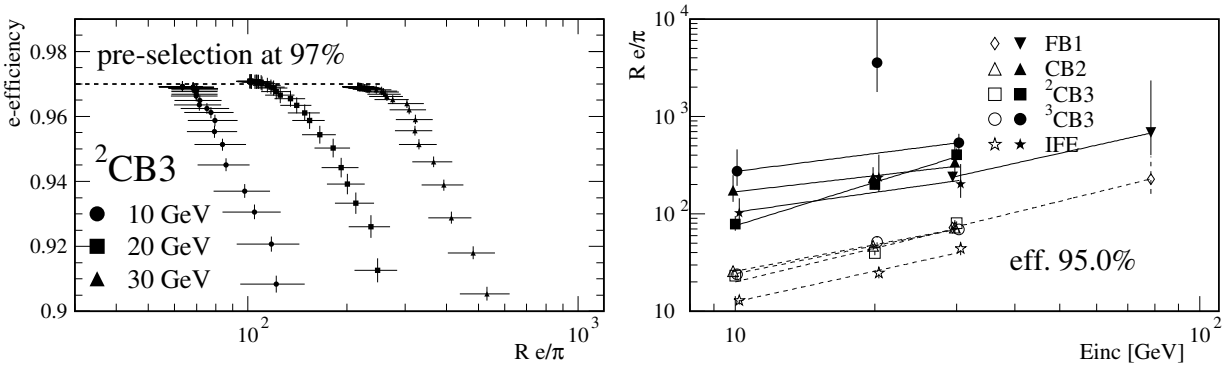

Figure 21: (a) ϵ_e *vs.* $R_{e/\pi}$ *for three energies in the* ^{2}CB3 *module.* (b) $R_{e/\pi}$ *at* $\epsilon_e = 95\,\%$ *as a function of* π *incident energy, obtained by combining pre-selection and the* ξ^2 *of the shower moments for all configurations* (full symbols). *The* open symbols *show* $R_{e/\pi}$ *obtained using only longitudinal estimators. The data of each module configuration are fitted to a straight line.*

first two elements of the vector $\vec{x}$. The results are also shown in fig. 21 (b). The rejection factors obtained are remarkably stable for the various configurations and vary smoothly with π incident energy. The IF module is slightly disfavoured here at the pre-selection level by the thickness of the $k = 0$ e.m. layer and the length (about $\sim 30\,X_0$ including dead materials in front) of the e.m. section. By comparing to the full combination, the transversal segmentation and the measurement of the transverse leakage of energy outside the cluster cone are seen to bring an improvement of ~ 4 (e.g. for FB1) to ~ 10 (e.g. or IF) of the π-rejection.

The π's surviving the combined pre-selection and shower moments rejection at a given ϵ_e, are strongly peaked toward their nominal incident energy, as was already seen after pre-selection in fig. 13 (b). That is to say that, as expected, it is much more difficult using pure calorimetric estimators to distinguish π's from e's when $E^\pi/E^\pi_{\rm inc} \simeq 1$. Nevertheless, the π-rejection can be further improved, especially towards low energy, if the information on incident particle momenta is provided independently by a tracking detector. This was studied indirectly for the FB1 data in [18] by introducing the measured total energy density ρ as an additional element of $\vec{x}$ assuming that it's strong dependence on incident momenta could be parametrized. This together with a full likelihood analysis comparing estimators of 30 GeV incident π only to those expected for 30 GeV e (independently of the measured π energy) gave rejection factors well above 10^3 at 95% ϵ_e.

For various physics applications, one is interested not only in the π-rejection for a π of a given energy to be accepted (i.e. misidentified) as an e at *any* measured energy as calculated in fig. 21 (b), but also at the resulting π-contamination *as a function* of the measured energy. The evolution with measured energy of the remaining π-contamination is very similar for the various data sets, and shown for example in fig. 22 for ^{3}CB3 data at 10, 20 and 30 GeV. The π-misidentification probability falls below 10^{-4} for $E^\pi/E^\pi_{\rm inc} < 0.7$ above 20 GeV. Beyond that, the essentially undistinguishable contamination of charge exchange reactions $\pi^+ n \rightarrow \pi^0 p$ occurring in the first ($k = 0$) e.m. layer starts to contribute significantly.

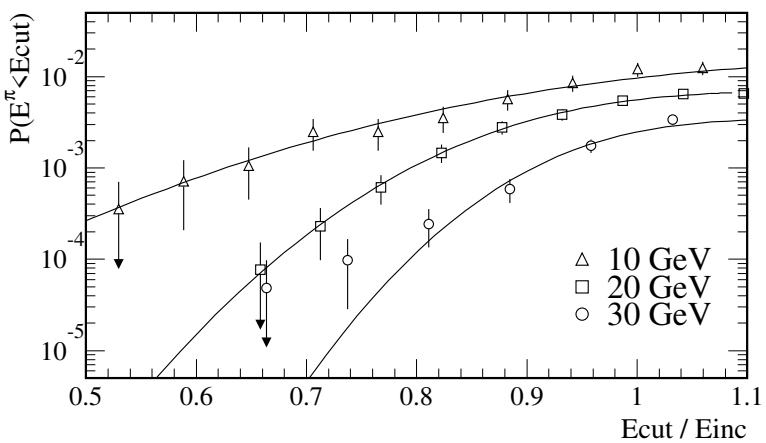

Figure 22: *Contamination probability $P(E^\pi < E_{\rm cut})$ for a π of energy $E_{\rm inc}$ to be misidentified as an e with energy below $E_{\rm cut}$, as a function of $E_{\rm cut}/E_{\rm inc}$ for ^{2}CB3 data at* 10, 20 *and* 30 GeV.

6 Conclusions

A study in H1 LAr calorimeter modules of electron energy measurements in the range 5 to 166 GeV, and electron identification in the energy range 10 to 80 GeV was presented.

Within an e.m. clustering envelope adapted to the characteristic size of electromagnetic showers, electrons are found to be measured with a fractional sampling resolution of $\sigma_E/E \simeq 11\,\%/\sqrt{E}$ and π-misidentification is suppressed to the $\sim 10^{-1}$ level (at 99 % ϵ_e) by the requirements of an early shower start, the presence of a dense energetic core or a proper longitudinal profile shape.

This contamination is further reduced by exploiting the hadronic shower leakage out of the electron envelope. In an isolation cone adapted to the characteristic size of hadronic showers, a Minimal Spanning Tree algorithm left a π-misidentification at the $\lesssim 10^{-2}$ level (97 % ϵ_e). A full combination of first and second longitudinal and transversal shower moments on top of pre-selection requirements, such as a large energy deposition in the electromagnetic section of the modules, diminishes further the probability for, e.g., 30 GeV pions to be misidentified as electrons of any measured energy to $\simeq 2 \rightarrow 5 \times 10^{-3}$. This probability falls to $\lesssim 10^{-4}$ for π's of energy $E_{\rm inc}$ to be misidentified as electrons at measured energy $E \lesssim 0.7 E_{\rm inc}$.

7 Acknowledgements

We wish to thank all technical collaborators who contributed to the construction and maintenance of the LAr calorimeters. The support of the CERN staff operating the H6 beam line is gratefully acknowledged. Finally, we thank all funding agencies for financial support.

References

[1] H1 Calorimeter Group, B. Andrieu et al., "The H1 Liquid Argon Calorimeter System", Nucl. Instr. and Meth. A336 (1993) 460.

[2] H1 Collaboration, I. Abt et al., "The H1 detector at HERA", DESY preprint 93-103 (July 1993).

[3] H1 Calorimeter Group, "... Calibration of the H1 Liquid Argon Calorimeter with Electrons", in preparation.

[4] H1 Calorimeter Group, B. Andrieu et al., "Results from pion calibration runs for the H1 Liquid Argon calorimeter ...", DESY preprint 93-047 (April 1993), to be published in Nucl. Instr. and Meth. A.

[5] H1 Calorimeter Group, B. Andrieu et al., "Electron identification in H1 lAr calorimeters", Proceedings of the 3rd Int. Conf. on Advanced Technology and Particle Physics, Como, Italy (June 1992), Nucl. Phys. (proc. Suppl.) B32 (1993) 97.

[6] P. Coet, "H6-Tertiary test beam", CERN EBS note 85-14; see also H.W. Atherton et al., CERN SPS note 85-43.

[7] C. Bovet et al., "The CEDAR counters for particle identification ...", CERN yellow report 82-13 (December 1982).

[8] H1 Calorimeter Group, W. Braunschweig et al., Nucl. Instr. and Meth. A265 (1988) 419.

[9] H1 Calorimeter Group, W. Braunschweig et al., Nucl. Instr. and Meth. A270 (1988) 334.

[10] E. Longo and I. Sestili, Nucl. Instr. and Meth. A128 (975) 283.

[11] S. Peters, "Die parametrisierte Simulation elektromagnetischer Schauer", Dissertation, Hamburg 1992, MPI-PHE 92-13 (September 1992).

[12] B. Michel (ALEPH Collaboration), Nucl. Instr. and Meth. A263 (1988) 43.

[13] CHARM II Collaboration, K. De Winter et al., Nucl. Instr. and Meth. A277 (1989) 170.

[14] A. Babaev et al., Nucl. Instr. and Meth. A160(1979)427.

[15] R. Engelmann et al., Nucl. Instr. and Meth. A216(1983)45.

[16] S. Abachi et al., D0 Collaboration, Nucl. Instr. and Meth. A324(1993)53.

[17] V. Boudry, "Recherche de leptoquarks dans l'expérience H1 auprès du collisionneur *e-p* HERA", Thèse de Doctorat, Université Paris VI (May 1992).

[18] M. Colombo, "Trennung von Elektronen und Pionen in einem Flüssigargonkalorimeter des H1 Detektors", Diplomarbeit, Universität Dortmund, (November 1990).